








RESEARCH ARTICLE

Deletion of aquaporin-4 improves capillary blood flow distribution in brain edema

Luca Bordoni^{1,2}  | Anna E. Thoren¹ | Eugenio Gutiérrez-Jiménez³  |
Knut S. Åbjørnsbråten¹ | Daniel M. Bjørnstad¹ | Wannan Tang^{1,4,5}  |
Mette Stern² | Leif Østergaard^{3,6}  | Erlend A. Nagelhus^{1†} |
Sebastian Frische²  | Ole P. Ottersen¹  | Rune Enger¹ 

¹GliaLab and Letten Centre, Division of Anatomy, Department of Molecular Medicine, Institute of Basic Medical Sciences, University of Oslo, Oslo, Norway

²Department of Biomedicine, Aarhus University, Aarhus, Denmark

³Center of Functionally Integrative Neuroscience (CFIN), Department of Clinical Medicine, Aarhus University, Aarhus, Denmark

⁴Department of Clinical and Molecular Medicine, Norwegian University of Science and Technology, Trondheim, Norway

⁵Department of Neurology, Neuroclinic, St. Olavs Hospital, Trondheim, Norway

⁶Department of Neuroradiology, Aarhus University Hospital, Aarhus, Denmark

Correspondence

Rune Enger, GliaLab and Letten Centre, Division of Anatomy, Department of Molecular Medicine, Institute of Basic Medical Sciences, University of Oslo, P.O. Box 1103 Blindern, N-0317 Oslo, Norway.
Email: rune.enger@medisin.uio.no

Funding information

Danish Medical Research Council, Grant/Award Number: 4004-00504; Højmosegårdlegatet, Grant/Award Number: 2017-1064/102 KBN; Aarhus University; European Union's Horizon 2020 Research and Innovation program under the Marie Skłodowska-Curie Actions Grant, Grant/Award Number: 80113; The Letten Foundation; The Olav Thon Foundation; Norges forskningsråd, Grant/Award Numbers: 302326, 249988, 262552; Helse Midt-Norge, Grant/Award Number: 28293; Felles forskningsutvalg (FFU), Grant/Award Number: 34226

Abstract

Brain edema is a feared complication to disorders and insults affecting the brain. It can be fatal if the increase in intracranial pressure is sufficiently large to cause brain herniation. Moreover, accruing evidence suggests that even slight elevations of intracranial pressure have adverse effects, for instance on brain perfusion. The water channel aquaporin-4 (AQP4), densely expressed in perivascular astrocytic endfeet, plays a key role in brain edema formation. Using two-photon microscopy, we have studied AQP4-mediated swelling of astrocytes affects capillary blood flow and intracranial pressure (ICP) in unanesthetized mice using a mild brain edema model. We found improved regulation of capillary blood flow in mice devoid of AQP4, independently of the severity of ICP increase. Furthermore, we found brisk AQP4-dependent astrocytic Ca²⁺ signals in perivascular endfeet during edema that may play a role in the perturbed capillary blood flow dynamics. The study suggests that astrocytic end-foot swelling and pathological signaling disrupts microvascular flow regulation during brain edema formation.

KEYWORDS

astrocyte endfoot, brain edema, Ca²⁺ signals, capillary blood flow, intracranial pressure

† Deceased.



1 | INTRODUCTION

Brain edema is associated with many disorders that affect the brain (Nehring et al., 2022). It is a condition in which fluid accumulation causes brain swelling and increased intracranial pressure (ICP) (Leinonen et al., 2017). In clinical settings, an increase in ICP above 22 mmHg defines a state of intracranial hypertension (Carney et al., 2017) and poses a life-threatening risk of brain stem herniation (Leinonen et al., 2017). However, it is now clear that even slight elevations of ICP may have adverse effects, particularly on capillary blood flow (Bordoni et al., 2021).

Not only the magnitude but also the distribution of capillary blood flow is important in determining oxygen delivery to the tissue (Angleys et al., 2015; Rasmussen et al., 2015). The flow distribution, referred to as the *capillary transit time heterogeneity* (CTH), can be estimated by both MRI and two-photon laser scanning microscopy (2PLSM) (Gutiérrez-Jiménez et al., 2016; Mouridsen et al., 2014). Under physiological conditions, flow distribution in the capillary bed will homogenize when blood flow increases, producing a lower CTH, which ensures efficient oxygen delivery to the brain (Angleys et al., 2015; Kleinfeld et al., 1998; Rasmussen et al., 2015). Active mechanisms involving the release of local vasoactive mediators (Longden et al., 2017; Uhlirva et al., 2016), changes in upstream arteriolar tone, and pericyte contractions or relaxations are thought to participate in this capillary flow regulation (Cai et al., 2018; Hall et al., 2014). During pathological conditions, a high CTH, reflecting unphysiological capillary blood flow heterogeneity, may impede oxygen delivery to the tissue (Østergaard et al., 2015). As CTH increases, tissue oxygenation is progressively uncoupled from blood flow (Angleys et al., 2015; Østergaard et al., 2015). In a situation with extremely inhomogeneous flow, oxygenated blood is essentially shunted through a small number of capillaries that act as a low resistance pathway into the venous circulation (Bragin et al., 2011).

During brain edema, both the signaling mechanisms and the structural integrity of the neuro-glio-vascular unit are perturbed (Stokum et al., 2016). For instance it has been shown that astrocytic endfeet swell (Bullock et al., 1991), due to their enrichment of the water channel aquaporin-4 (AQP4) (Amiry-Moghaddam et al., 2003; Manley et al., 2000; Nielsen et al., 1997; Thrane et al., 2011; Vajda et al., 2002, 2004). Swelling of endfeet may be detrimental for blood flow dynamics both by structural compression of the capillaries, and by interfering with vasoactive signaling mechanisms affecting endothelial cells and pericyte contractility (Østergaard et al., 2014). A key signaling pathway involved is astrocytic Ca^{2+} signaling. In anesthetized mice, Ca^{2+} signals increase prominently in the somata of astrocytes during brain edema development in an AQP4-dependent manner (Thrane et al., 2011). Anesthesia, however, severely perturbs astrocytic Ca^{2+} imaging, and the field is undergoing a revolution as recent technological advances has enabled the study of these signals in awake unanesthetized mice (Thrane et al., 2012). Similarly, cerebral blood flow regulation (Slupe & Kirsch, 2018) and ICP (Eftekhari et al., 2020) is known to be profoundly affected by

anesthesia. Therefore, there is a need to investigate these mechanisms without the detrimental effects of anesthesia.

Using 2PLSM of mice subjected to water intoxication causing mild cytotoxic brain edema (Bordoni et al., 2021) with preserved blood brain barrier integrity (Adler et al., 1993; Melton et al., 1987), we show in non-anesthetized mice that capillary flow dynamics are profoundly affected during brain edema formation, and that removal of AQP4 significantly improves flow dynamics at any level of ICP increase. Moreover, we find reduced astrocytic Ca^{2+} signaling in perivascular astrocytic endfeet in mice devoid of AQP4, suggesting a role for endfoot Ca^{2+} in regulating microvascular flow dynamics in edema. Altogether, these findings suggest that inhibition of AQP4 activity during the formation of brain edema could improve capillary flow dynamics and tissue oxygenation.

2 | RESULTS

2.1 | *Aqp4*^{-/-} mice develop less severe brain edema during mild water intoxication

In this study, we used mild water intoxication, causing a ~15% decrease in plasma osmolarity compared to mice injected with an equal volume of saline (Figure 1a). Mice were only mildly hyponatremic before sacrifice ($\text{Na}^+ = 132.3 \pm 3.6$ and 132.4 ± 2.9 for wildtype (WT) and *Aqp4*^{-/-}, respectively, Figure 1c). To estimate the severity of brain edema, we measured brain water content by wet weight/dry weight difference. Similarly to previous reports (Haj-Yasein et al., 2011; Li et al., 2013), we observed a higher basal brain water content in *Aqp4*^{-/-} mice (Figure S1). However, the increase in brain water content following water intoxication was significantly lower in *Aqp4*^{-/-} mice than WT mice compared to mice receiving only saline ($\Delta = 0.33 \pm 0.15\%$, $p = .031$) (Figure 1b).

2.2 | Capillary blood flow during edema

To assess changes of capillary blood flow during brain edema, we imaged an intravenously injected bolus of fluorophore (70,000 MW Texas Red-labeled dextran) on the arterial and venous side of the capillary bed by 2PLSM (Figure 1a,d). The delay and widening of the fluorescent signal by the capillary network was then modeled by a cumulative gamma distribution (Gutiérrez-Jiménez et al., 2016; Mouridsen et al., 2014), from which plasma mean transit time (MTT) and CTH was estimated at 6 different time points before and after water intoxication (Figure 1e).

Despite using a mild model of brain edema, we observed a significant increase in MTT already at ~15 min from water intoxication in both genotypes (+40% and +59% for WT and *Aqp4*^{-/-} mice, $p < .001$ for both) (Figure 1f). Decreased capillary blood flow persisted throughout the whole experiment and was similar in the two groups (WT: 74% maximal increase in MTT; *Aqp4*^{-/-}: 75% maximal increase in MTT).

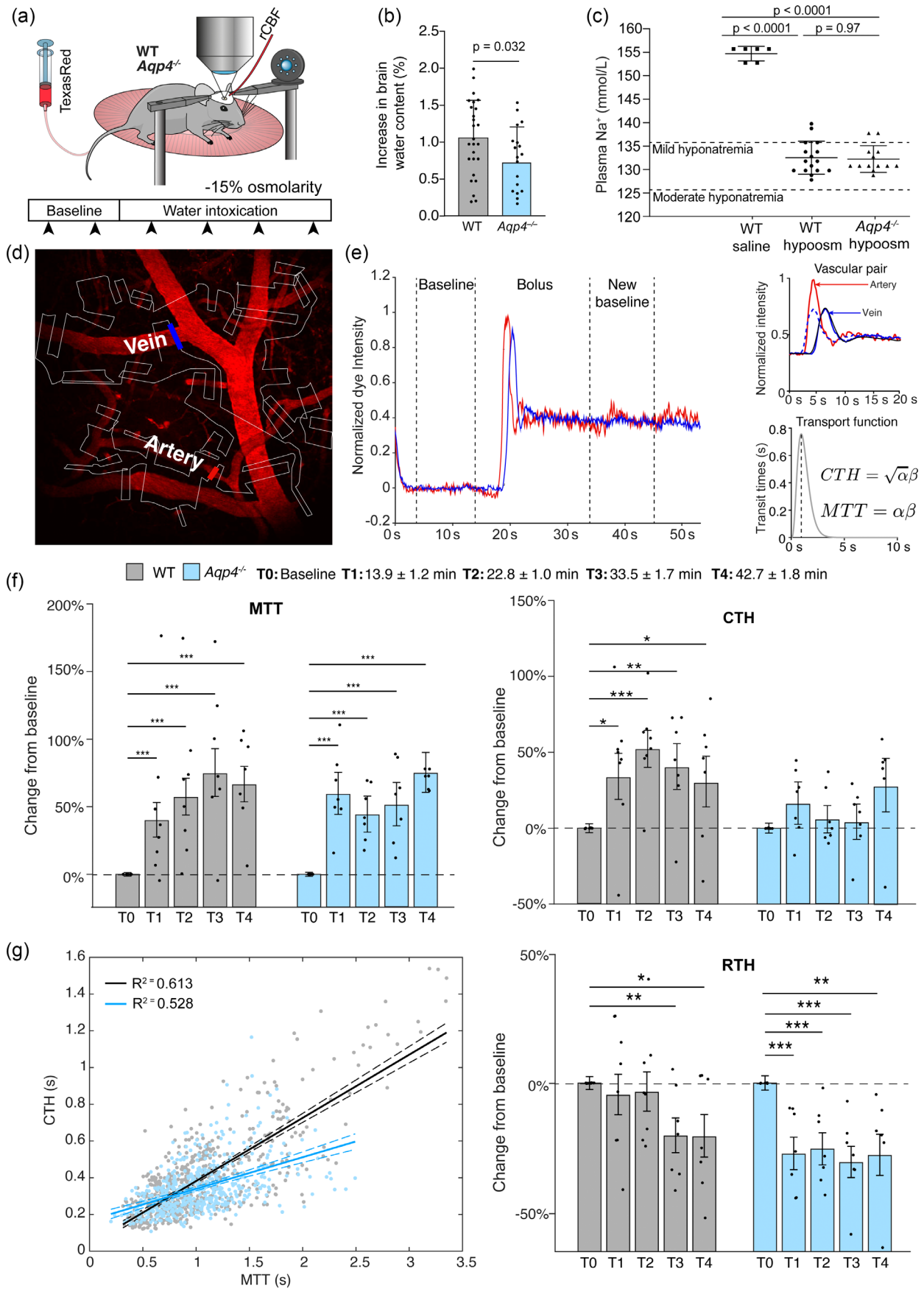


FIGURE 1 Legend on next page.



2.3 | Improved capillary flow distribution and regulation in *Aqp4*^{-/-} mice

Brain edema caused a pronounced and similar reduction of capillary blood flow (increase in MTT) in both genotypes. However, when assessing blood flow distribution, we identified clear differences between the genotypes (Figure 1f,g): WT mice had a significant increase in blood flow heterogeneity during edema formation (CTH: first significant increase from baseline at ~15 min, $p = .012$, peak: 52% increase in CTH at ~20 min, $p < .001$) that persisted until the end of the experiment. Conversely, we observed no significant difference from baseline in *Aqp4*^{-/-} mice at any time point, indicating a more homogeneously distributed blood flow.

In a capillary network that is not under active regulation, MTT and CTH would vary so that their ratio (CTH/MTT = relative transit time heterogeneity, RTH) is maintained constant (Rasmussen et al., 2015). Changes in RTH can be observed with blood flow increases during neurovascular coupling (Gutiérrez-Jiménez et al., 2016). Also, during pathological conditions such as in the penumbra of a cerebral infarction, capillary network malfunction would lead to a change in RTH (Engedal et al., 2018; Østergaard et al., 2015). RTH can thus be considered an index of the ability of the capillary network to actively homogenize its flow.

We observed significant changes in RTH during edema development (Figure 1g). In WT mice, RTH did not significantly change until the late phase of the edema progression (at ~30 and ~40 min after water intoxication), decreasing by 21% at both time points ($p = .009$ and $.03$, respectively). Conversely, in *Aqp4*^{-/-} mice, RTH had dropped already in the first time point after water intoxication (27% reduction in RTH at ~15 min, $p < .001$ compared to baseline) and remained reduced throughout the experiment (25% to 31% reduction at T3 and T4, respectively, $p < .001$ compared to baseline for both). These findings suggest that the active mechanisms of capillary flow distribution regulation are better preserved in *Aqp4*^{-/-} during brain edema. The difference between the genotypes was not dependent on MTT but rather on a significantly higher CTH for every value of MTT during edema in WT mice (Figure 1g, left. Slope: 0.34 vs. 0.17 in WT vs. *Aqp4*^{-/-} mice, $p < .001$).

Next, we assessed diameters of microvessels in volumetric Z-stacks, using DeepVess (Haft-Javaherian et al., 2019), a convolutional neural network for segmenting the vasculature (Figure S2A). We found a

reduction in microvascular diameters in brain edema in WT mice, but no change in *Aqp4*^{-/-} mice, but no change in the coefficient of variation of diameters (Figure S2A). We also assessed perfusion in individual microvessels by using 2PLSM linescans (Figure S2B–H) and observed that intracapillary flux was significantly decreased in both genotypes (Figure S2D). Interestingly, the coefficient of variation of intracapillary flux increased in WT mice (Figure S2E), but remained unchanged in *Aqp4*^{-/-} mice, suggesting more heterogeneous flow dynamics in WT mice during edema. In addition, linear density of RBCs (RBC/mm capillary, Figure S2F) was significantly increased in *Aqp4*^{-/-} mice (+22% and +30% relative increase from baseline at ~10 and ~50 min from water intoxication, respectively, $p < .05$ for both), and higher than in WT mice (~50 min after edema: 45.5 ± 4.0 vs. 67.2 ± 7.4 , mean \pm standard error, $p < .01$). Capillary RBC velocities did not change over time in either genotype (Figure S2G–H). Altogether, the higher number of RBC per unit of capillary length during edema and more homogenous flow in *Aqp4*^{-/-} mice suggests a healthier microcirculation and is expected to improve tissue oxygenation.

2.4 | AQP4 affects ICP and blood flow during mild water intoxication

After showing that capillary blood flow progressively worsened after water intoxication and that the presence of AQP4 led to more heterogeneous capillary blood flow, we investigated how macrovascular parameters influence capillary blood flow and distribution. Thus, we quantified ICP and regional cerebral blood flow (rCBF, by laser Doppler flowmetry) (Figure 2a,b). Baseline values of both ICP and rCBF (Figure 2d,e) were similar between the two genotypes, and in WT controls injected with saline (Figure S3A). After mild water intoxication, however, ICP and rCBF changed with a different rate and reached a different maximal change in WT and *Aqp4*^{-/-} mice (Figure 2c–e). In WT mice, ICP increased beyond the threshold of cranial hypertension of 22 mmHg at 20 min after water intoxication and reached a plateau at 32.1 ± 2.65 mmHg at ~40 min. Conversely, in *Aqp4*^{-/-} mice, we found both a slower rise rate (Figure 2g) and a lower final plateau level (21.4 ± 3.9 mmHg). More specifically, both the cumulative ICP (Figure 2d) and the rate of ICP elevation in the first 10 min after water intoxication (mmHg/min in Figure 2g) were significantly different between

FIGURE 1 Changes in capillary flow dynamics during mild water intoxication. (a) Experimental setup. WT and *Aqp4*^{-/-} mice were fitted with a cranial window exposing somatosensory cortex. After 3 weeks of recovery, a tail vein catheter for bolus injections of 70,000 MW Texas Red-labeled dextran was implanted. rCBF: regional cerebral blood flow, measured by laser Doppler flowmetry. Following a baseline of 1 h, mice were injected with 10% of the body weight hypotonic solution. (b) Increase in brain water upon hypoosmotic challenge compared to sham (WT: $n = 26$ mice, *Aqp4*^{-/-}: 18 mice, unpaired t -test). (c) Plasma Na⁺ levels after hypo-osmotic challenge. The cutoff for mild and moderate hyponatremia indicated by stippled lines (WT: $n = 16$, *Aqp4*^{-/-}: $n = 13$ mice, WT saline: $n = 6$ mice, one-way ANOVA). (d) 2PLSM of cortical vessels, outlining a pial artery and vein supplying and emptying the capillary bed (e) Left: Example fluorescence from a pial artery (red) and a pial vein (blue) for one bolus injection. Right: The passage of the fluorescent dye from the arterial to the venous network was modeled by a cumulative gamma distribution. From the free parameters α and β of the distribution, MTT and CTH were estimated as $\alpha\beta$ and $\sqrt{\alpha\beta}$, respectively (Gutiérrez-Jiménez et al., 2016). (f) Relative changes of MTT and CTH at different time points after water intoxication. (g) (Left) Linear regression of CTH versus MTT. Stippled lines: 95% confidence interval. (Right) Relative transit time heterogeneity (RTH) at different time points after edema initiation. Bars represents estimates and standard errors from generalized linear mixed effects modeling. $n =$ WT: 131 measurements in 8 mice; *Aqp4*^{-/-}: 121 measurements in 7 mice. * $p < .05$; ** $p < .01$; *** $p < .001$.

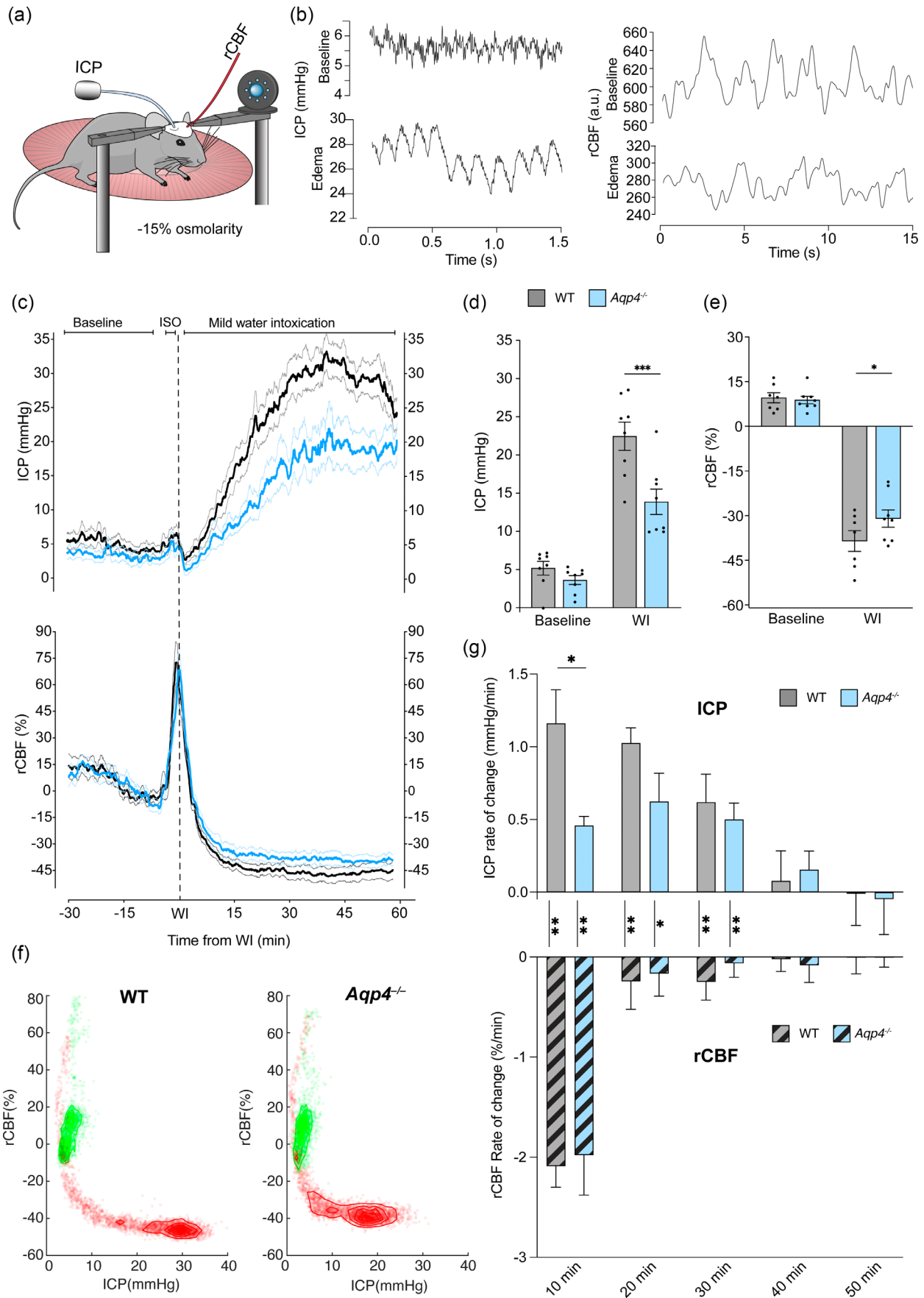


FIGURE 2 Legend on next page.

genotypes (8.58 ± 1.90 mmHg difference between the genotypes, $p < .001$ in Figure 2d, and 0.70 ± 0.24 mmHg/min difference between the genotypes, $p = .018$ in Figure 2g). Overall, consistent with previous studies in anesthetized mice using more severe brain edema models (Yang et al., 2008), AQP4 acts as a rate-limiting factor during edema formation. rCBF significantly decreased after mild water intoxication (Figure 2c bottom, e, g) in both genotypes, reaching a plateau of $-44.6 \pm 3.5\%$ and $-35.6 \pm 3.96\%$ already within 15 min., with a small and marginally significant difference between the genotypes in accumulated rCBF reduction after WI ($+7.56 \pm 3.49\%$ in WT compared to $Aqp4^{-/-}$, $p = .04$, Figure 2e). Conversely, there was no difference in rCBF rate of change at any time point.

2.5 | Non-linear relationship between ICP and rCBF after mild water intoxication

Based on the relationship between ICP, cerebral perfusion pressure, and CBF (Madhok et al., 2018), we hypothesized that the increase in ICP during edema was tightly correlated to, and likely the cause of the reduction in rCBF. Unexpectedly, this correlation was not confirmed experimentally (Figure 2f,g). In both genotypes, more than 80% of the total decrease in CBF was observed within the first 10 min after water intoxication, whereas ICP was only modestly increased in the same time range (Figure 2g). Conversely, ICP continued to increase the first 30 min from mild water intoxication in both genotypes, where no decrease in rCBF was observed.

Furthermore, by visualizing the relation between ICP and rCBF in a 2D-density plot (Figure 2f), we noticed that rCBF values approaching the plateau level were observed even at $ICP = 10$ mmHg, approximately $\frac{1}{3}$ and $\frac{1}{2}$ of the final plateau level of the ICP in WT and $Aqp4^{-/-}$, respectively. Overall, our results in awake mice shows that high ICP does not determine the reduction in CBF observed during the progression of brain edema.

2.6 | The effect of ICP and rCBF on capillary flow dynamics

We found a highly non-linear relationship between ICP and rCBF changes during edema formation. In order to understand how ICP and

rCBF correlated with capillary blood flow dynamics, we predicted mean ICP and rCBF for each min following mild water intoxication (same data as in Figure 2c) and performed a linear regression to each value of MTT, CTH, and RTH based on the time from edema of individual bolus tracking scans.

In WT mice, ICP within a range from 0 to 25 mmHg, but not rCBF, was a significant predictor of both MTT and CTH values (slope: 0.035 and 0.012, respectively, $p < .001$ for both), but not of RTH (Figure 3, Table S1 and Figure S4). In WT mice during edema, capillary flow changed as would be expected in a passive compliant flow system with constant RTH resulting from a parallel increase in CTH and MTT. In $Aqp4^{-/-}$ mice, similar results were observed for MTT as in WT mice, whereas CTH remained unchanged and RTH decreased (slope: 0.06, $p = .0013$) as a function of increasing ICP. Therefore, the same degree of ICP predicts a significantly lower CTH and lower RTH in the absence of AQP4.

2.7 | Astrocytic endfoot hyperactivity during brain edema development

Brain capillaries are ensheathed by astrocytic endfeet, a specialized type of astrocytic process heavily enriched with AQP4, and only small discontinuities are present (Mathiesen et al., 2010). Since astrocytic endfeet swell during brain edema (Bullock et al., 1991), potentially compressing the microvasculature, we then investigated whether astrocytic endfoot Ca^{2+} transients could represent a molecular substrate for the changes in capillary dynamics we observe. To do this, we used recombinant adeno-associated virus and the *GFAP* promoter to target *GCaMP6f* to astrocytes (Enger et al., 2019). After at least 3 weeks of recovery after surgery, mice were subjected to water intoxication, and 2PLSM 2D time series were acquired (Figure 4a). The resultant imaging data were analyzed with an event-based astrocytic Ca^{2+} signaling analysis method, the region-of-activity (ROA) algorithm from the Begonia toolbox (Bjørnstad et al., 2021) (Figure 4b). This method uses noise-based thresholding of individual pixels over time to separate signal from noise. Adjoining pixels in time and space with signal are then connected to form ROAs.

We found that brain edema in awake WT mice induced brisk increases in astrocytic Ca^{2+} signaling compared to baseline

FIGURE 2 ICP and rCBF dynamics during brain edema. (a) Experimental setup. A hollow PLA screw connected to a PE-20 5 mm cannula was implanted through the skull overlying somatosensory cortex in WT and $Aqp4^{-/-}$ mice. After 2 weeks of recovery, a pressure sensor (PA-C10, DSI) was inserted through the cannula. The laser Doppler fiber was placed on the contralateral side of the ICP sensor. The same edema protocol as the 2PLSM group was used. (b) Representative ICP and rCBF waveforms during baseline and 30 min after water intoxication. In both traces, arterial pressure-derived pulsatility appeared at approximately 7–10 Hz. At elevated ICP levels we observed an increased systole-to-diastole pressure difference. (c) ICP (mmHg) and rCBF (% change from baseline) traces. Stippled line: water injection. The quick exposure to anesthesia had negligible effects on ICP, but it induced a strong but brief response in rCBF. Traces represent mean \pm SEM. For ICP, $n = 8$ mice for both genotypes. For rCBF, $n = 7$ and 8 mice for WT and $Aqp4^{-/-}$. (d–e) Cumulative ICP and rCBF during baseline and after water intoxication. Mean \pm SEM with each mouse overlaid. Statistical Analysis: two-way paired ANOVA. (f) Density contour plot of ICP versus rCBF. Individual points: mean value from all ICP and rCBF traces for the same time point after water intoxication Green: baseline ($n = 1800$). Red: water intoxication ($n = 3473$). Same number of subjects as in (c). (g) Rate of change by min for ICP (top) and rCBF (bottom), mean \pm SEM of the rate of change in time blocks of 10 min from edema. Statistical analysis: two-way repeated measurement ANOVA. * $p < .05$; ** $p < .01$; *** $p < .001$.

FIGURE 3 Linear regression of ICP and capillary flow parameters after water intoxication for WT (black) and *Aqp4*^{-/-} mice (blue). Sample size is the same as in Figure 1f.g. For every MTT, CTH and RTH measurements, we calculated the predicted ICP based on the time after edema of each bolus tracking scan.

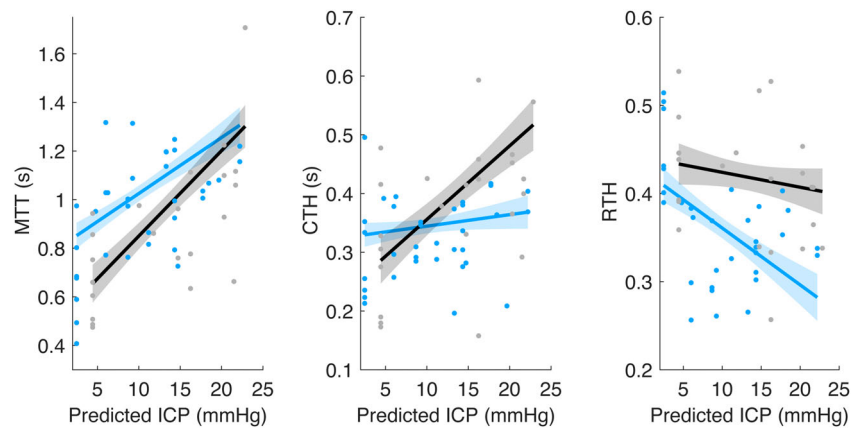


(Figure 4c,d). Specifically, the fraction of active pixels in the FOV (the ROA density) and the frequency of Ca^{2+} events (ROA frequency) were significantly higher at each time point after water intoxication. Conversely, Ca^{2+} signaling remained unchanged in *Aqp4*^{-/-} mice after the hypo-osmotic challenge.

In vitro experiments have shown that the astrocytic response to hypo-osmotic challenge is heterogeneously distributed across the cellular subcompartments (Eilert-Olsen et al., 2019). Therefore, we measured ROA density and frequency in the three distinct astrocytic subcellular compartments – somata, glial processes, and endfeet – to assess which regions of the astrocyte were the most active after water intoxication. In WT mice, Ca^{2+} activity in the glial somata was unchanged during edema, while both processes and endfeet displayed a significant increase in signaling. In *Aqp4*^{-/-} mice, no subcellular compartments showed any increase in Ca^{2+} activity during edema, while a small but significant reduction in Ca^{2+} signal was observed in somata and processes, but not in endfeet, in the first time point after water intoxication. Overall, we have shown that the hypo-osmotically induced increase in Ca^{2+} activity in astrocytes during brain edema resides within the astrocytic processes and astrocytic endfeet.

3 | DISCUSSION

In this work, we found perturbed capillary blood flow dynamics in unanesthetized mice undergoing mild brain edema (Bordoni et al., 2020). Moreover, the removal of AQP4 water channels played a beneficial role for microvascular blood flow, in addition to its general effects on edema formation, affecting how the capillary network adapts to changes in blood flow to support tissue oxygen availability. Finally, we demonstrated brisk AQP4-dependent Ca^{2+} signaling in the astrocytic endfeet, potentially shedding light on the mechanistic underpinnings of the observed vascular dysfunction.

Using fluorescence bolus-tracking by 2PLSM (Gutiérrez-Jiménez et al., 2016), we estimated capillary flow (MTT), homogeneity of flow (CTH), and the relationship between these two measures (RTH). Despite a similar MTT in the two genotypes, the capillary flow

distribution (CTH) was highly different in the two groups as edema progressed. In WT mice, CTH increased by about 50% compared to baseline, whereas in *Aqp4*^{-/-} mice, no time points were different from baseline. The increase in MTT without a concomitant increase in CTH produced a faster and lasting reduction in RTH in *Aqp4*^{-/-} mice, which together with the increased capillary linear density, likely mirrors active regulatory mechanisms that preserve capillary flow dynamics and improve oxygen extraction.

In the late stage of pathological conditions associated with severe flow-restriction, as within the ischemic penumbra in stroke, low RTH values may indicate widespread collapse of the capillary network (Engedal et al., 2018). Also during brain edema, elevated ICP even within a moderate range (15–22 mmHg) could reduce the number of perfused brain microvessels (Bordoni et al., 2021; Bragin et al., 2011). We were not able to accurately detect capillary stalling in our study, and future studies using more high throughput imaging modalities like optical coherence tomography should be performed (Bordoni et al., 2021). It is unlikely that the lower RTH we observed in *Aqp4*^{-/-} mice originates from widespread microvascular collapse, since the reduction in RTH and low CTH occurred early in the edema progression, prior to any significant pathological increase in ICP. Moreover, in WT mice, which do experience a pathological increase in ICP earlier than *Aqp4*^{-/-} mice, we saw an increase in CTH, not a reduction (Engedal et al., 2018).

We demonstrate a pronounced increase in astrocytic Ca^{2+} signaling during edema, which is an important signaling pathway involved in cellular volume regulation, and likely plays a role in the control of capillary flow (Krogsgaard et al., 2022; Mishra et al., 2016). Our findings are consistent with a previous study using synthetic Ca^{2+} indicators in anesthetized mice (Thrane et al., 2011). However, we found a considerably higher level of Ca^{2+} activity, further stressing the importance of studying mice without the confounding effects of anesthesia. We cannot rule out dilutional effects of intracellular Ca^{2+} levels or GCaMP6f levels in our model, but believe the effect is marginal because of the relatively mild osmotic challenge and because the baseline for detecting Ca^{2+} signals is calculated for each of the Ca^{2+} imaging recordings, compensating for slow drifts in baseline fluorescence throughout the experiment. Future studies quantitatively assessing intracellular Ca^{2+} concentrations are warranted.

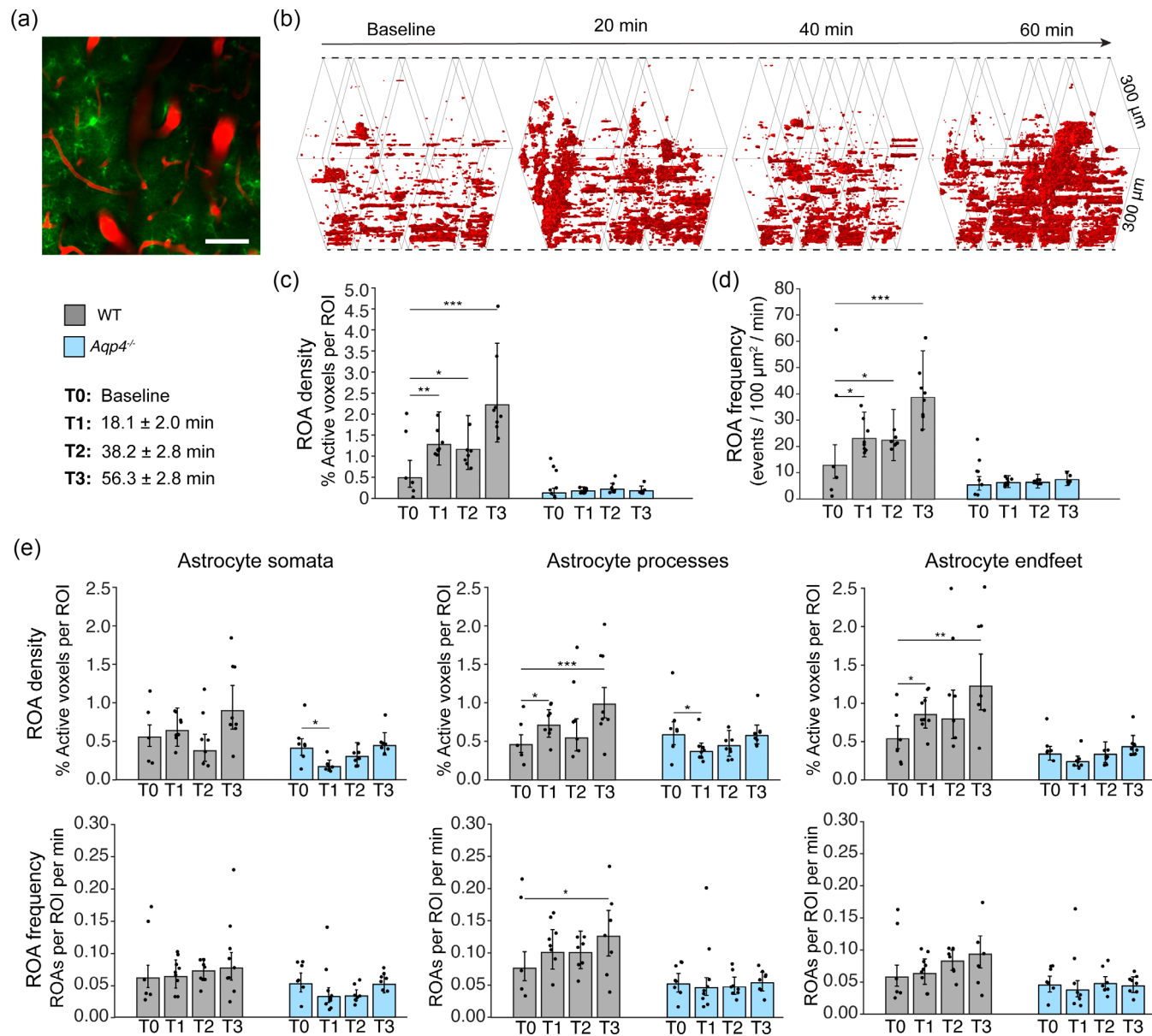


FIGURE 4 Astrocytic Ca^{2+} signaling during brain edema is most clearly confined to glial processes and endfeet. (a) Example field-of-view at 150 μm below the brain surface in somatosensory cortex. 3 weeks prior to water intoxication, mice were transfected with rAAV-GFAP-GCaMP6f (green). The vasculature was outlined by 70,000 MW Texas Red-labeled dextran (red). Scale Bar: 30 μm . (b) Astrocytic Ca^{2+} signals were analyzed with the event-based ROA method (Bjørnstad et al., 2021). Adjoining active voxels in space and time were joined and visualized in a 3D rendering with Ca^{2+} activity in red. As brain edema develops the density of ROAs increases. (c–d): ROA density (percent active voxels within a compartment) and frequency (number of events/ $100 \mu\text{m}^2/\text{min}$). Both ROA density and frequency were significantly higher than baseline for any time after edema in WT (gray), but not in $Aqp4^{-/-}$ mice. (e) ROAs within manually drawn regions-of-interest (ROI) defining astrocytic somata, processes, and endfeet around capillaries. For c–e, Data are presented as estimates \pm standard error. WT: $N = 9$ mice, $Aqp4^{-/-}$: $N = 8$ mice, 1 FOV per mouse for both genotypes. ROIs for WT and $Aqp4^{-/-}$ respectively: $n = 616$ and 421 somata, 231 and 201 processes, 673 and 575 endfeet. Statistics were performed with generalized linear mixed models analyses, where ROA density and frequency were considered the response variables, and time from water intoxication, genotype, and subcellular region (only in e) were considered fixed effects, and mouse identity was considered a mixed effect. * $p < .05$; ** $p < .01$; *** $p < .001$.

We find a reduction in microvascular diameters during edema in WT mice, but not in $Aqp4^{-/-}$ mice, which may represent either a structural compression of the microvasculature or altered microvascular blood flow regulation. In our Ca^{2+} imaging recordings, we were not able to directly assess endfoot volume changes. However, it is known

that astrocytic endfeet swell in brain edema, compressing the capillary lumen and impeding RBC passage (Amiry-Moghaddam et al., 2003; Bullock et al., 1991; Manley et al., 2000). The consequences of such swelling is illustrated by the beneficial effect of treating brain edema with intravascular hyperosmolar solution, an effect that has been

shown to be dependent on perivascular AQP4 (Nakayama et al., 2016). In the present study, we localized for the first time increased AQP4-dependent Ca^{2+} signaling to the astrocytic capillary endfeet, suggesting a signaling mechanism in addition to structural compression that can be involved in perturbed capillary flow dynamics in edema. It is tempting to speculate that the endfoot Ca^{2+} signaling is triggered by endfoot swelling, for instance activating the stretch-sensitive Ca^{2+} channel transient receptor potential vanilloid 4 (TRPV4) (Benfenati et al., 2011).

Anesthesia is not only detrimental for astrocytic signaling, but also represents a grave challenge for physiological homeostasis in rodents. The combined effects of surgical trauma, unphysiological blood gas values, and inaccurate temperature control could severely perturb any brain process, in particular blood flow control (Slupe & Kirsch, 2018). In this study, we aimed to lift these confounding effects by studying awake-behaving mice with chronic surgical implants and, to the best of our knowledge, this is the first study measuring ICP in un-anesthetized mice. Surprisingly, we found a highly non-linear relationship between ICP and rCBF. This uncoupling between ICP and CBF may be explained by cerebral autoregulation mechanisms (Bragin et al., 2016; Johnston et al., 1973), which are known to be affected by anesthesia in a dose-dependent manner (Slupe & Kirsch, 2018). Together with recent studies chronically measuring ICP on awake rats (Eftekhari et al., 2020; Guild et al., 2015), our observations underscore the importance of studying mice without the confounding effects of anesthesia whenever possible.

In this study using mild water intoxication, not only did we confirm in non-anesthetized mice that the removal of AQP4 reduces the overall brain water increase and ICP accumulation during brain edema, but we also observed a significantly more homogeneous capillary blood flow given any level of ICP increase. Altogether, these findings suggest that inhibition of AQP4 activity during the formation of brain edema could improve capillary flow dynamics and tissue oxygenation. Our quantification of Ca^{2+} signals in astrocytes suggests a potential role for endfoot Ca^{2+} signaling in regulating microvascular flow dynamics in edema. Several mechanisms during the development of edema can collectively impede the function of brain microvessels, and to elucidate their individual contribution and kinetics should be a subject of future studies. In particular, assessing the effect of the selective AQP4 inhibitors TNG-020 (Toft-Bertelsen et al., 2021) and the newly developed AER-271 (Farr et al., 2019) on microvascular blood flow is warranted.

4 | MATERIALS AND METHODS

4.1 | Animals

Male C57BL6/J from Janvier Labs (WT mice) and *Aqp4*^{-/-} mice of 13–22 weeks of age (weight: 25–33 g) (Thrane et al., 2011) were used. Mice were housed in controlled conditions of humidity (1–3 mice per cage), temperature, and with a standard light–dark cycle (8:00–20:00), and had ad libitum access to food and water. The home cages were enriched with running wheels, biting sticks, and cardboard tubes. All procedures were carried out in accordance with the European Animal

research law (Directive 2010/63/EU) and with approval from Norwegian Food Safety Authority (Mattilsynet – FOTS 12006).

4.2 | Mild water intoxication and endpoint measurements

Mice underwent mild water intoxication (WI) as previously described (Bordoni et al., 2020). Briefly, mice were injected with a 30.8 mM NaCl solution (1:5 dilution of saline in MilliQ water), 10% body weight intraperitoneally. Sham mice received 10% body weight of saline. WI solution was kept at 37°C and administered over 30 s under brief isoflurane anesthesia. Mice were monitored for 1 h after the hypoosmotic infusion and then euthanized by decapitation during anesthetic overdose (ZRF: 18.7 mg Zolazepam, 18.7 mg Tiletamine, 0.45 mg Xylazine and 2.6 µg fentanyl, 300 µL). Before euthanasia, an arterial blood sample was obtained to measure plasma sodium (ABL 90FLEX, Radiometer, Denmark). Brain water content was measured with wet weight/dry weight ratio, after separation of brain stem, mechanical homogenization using a spatula on a glass coverslip, and a 24 h 110°C desiccation protocol.

4.3 | Surgery and virus transduction

Animals were anesthetized with isoflurane (3% for induction and 1.25%–1.5% for maintenance) using a mixture of room air and pure oxygen (50% pure oxygen, 50% room air) and buprenorphine, (0.1 mg/kg i.p.). After induction, the mouse was fastened in a stereotaxic frame on a nose cone (Model 963, KOPF Instruments). Body temperature was maintained at 37°C by a temperature-controlled heating pad. Eyes were protected with ointment and the surgical area was disinfected with iodine solution (2%). Local analgesia (bupivacaine, 5 mg/mL) was injected subcutaneously at the site of surgery.

The skull was exposed, cleaned from connective tissue, and grooves were carved on all exposed periosteum with a scalpel in a checkerboard pattern to strengthen the adhesion between bone and cyanoacrylate glue. A craniotomy of 2.5 mm diameter was made as previously described (Enger et al., 2017), centered at 2.0 mm lateral and 1.5 mm posterior from Bregma. The skull was carefully drilled using a dental drill with intermittent soaking.

The production of rAAV-GFAP-GCaMP6f was done as previously described (Bojarskaite et al., 2020; Tang et al., 2015). The virus was stereotactically injected via a glass capillary (70 nL at 35 nL/min) in two locations at 150 µm depth from the brain's surface.

The craniotomy was sealed differently in the 2PLSM and ICP-measurement mice. In 2PLSM mice, a cranial window made of 2 layers of circular coverslips (2.5 mm and 3.5 in diameter for lower and upper layer) glued together by ultraviolet-curing glue (Norland Optical Adhesive No. 61) was positioned on the exposed dura (Huber et al., 2012). The glass window was fixed to the skull by cyanoacrylate-gel glue (Loctite-super glue gel) and reinforced with dental cement (Meliodent, Kulter).



In ICP-LD mice, a custom hollow PLA screw (outer diameter: 3 mm, inner diameter: 0.51 mm, Shaft: 0.2 mm) was attached to a 5 mm long polyethylene tube (PE 50, Intramedic Clay Adams) with dental cement (GC Fuji PLUS) and filled with sterile saline. After the removal of the bone flap, the screw was positioned over the brain until clear, heart-rate driven pulsations from epidural ICP were observed in the liquid interphase inside the tube. The outer perimeter of the screw was glued to the skull with cyanoacrylate glue and sealed with impression material (Take 1 Advanced, Keer Dental). After sealing of the craniotomy, a layer of liquid cyanoacrylate glue (Loctite) was applied to all exposed areas of the skull. Before complete air-curing, a plastic probe holder (Model: PH 07-7, Perimed) for LD measurements was positioned on the contralateral hemisphere above the right-middle cerebral artery (ML: +3 mm, AP: +2 mm). A titanium head bar was fastened over the occipital bone with cyanoacrylate glue. All implants were firmly secured to the skull with dental cement (Meliodent, Kulter).

Postoperative analgesia (meloxicam, 2.4 mg/kg, and buprenorphine, 0.1 mg/kg) was administered once per day for 3 days after surgery. Habituation started 7 days after surgery for LD-ICP animals and 14 days after surgery for 2PLSM animals. Each mouse underwent 4–8 habituation sessions of 20 min. Training was concluded when mice reached a secure running pace and no gait instability on the rotating disc.

4.4 | ICP and rCBF measurements

Mice were briefly (<15 min) prepared for the experiment under isoflurane anesthesia (2%) and buprenorphine (0.1 mg/kg). The lumen of the PE 50 tube was gently flushed with saline until heart-beat driven ICP pulsations were observed. Isoflurane was discontinued and the mouse was head-fixed for 30 min before any measurement.

ICP was sampled at 500 Hz with a pressure telemeter (PA-C10, Data Science International – DSI). Data were recorded on DataQuest ART 4.31. Accuracy of the measured ICP trace was improved by barometric-adjustment with an Ambient Pressure Reference (APR-2, DSI) and by adjusting the pressure sensor offset before each experiment. The ICP probe was inserted into the probe holder and the tip of the pressure sensor was carefully advanced through the epidural canula until dura was reached. To avoid potential misplacements of the probes and pressure loss, the whole skull was covered with impression material (Silagum Mono, DMG). Measurements started 30 min after probe insertion. The tip of the implant was re-gelled and sterilized with 1% Terg-A-Zyme solution after each experiment.

rCBF was sampled at 32 Hz sampling rate by a LD probe (PF 5010, Periflux System 5000, Perimed). Data was recorded with PeriSoft (Perimed). Before the experiment, a small amount of vaseline was applied on the tip of LD fiber optic probe (Probe 407, Perimed) to facilitate the insertion in the PH 07-7 probe holder on the mouse skull. Data were recorded with PeriSoft (Perimed).

Infrared-sensitive video and wheel movements were simultaneously recorded using a LabVIEW interface (National Instruments). Recording protocol: (1) Baseline (40–60 min); (2) Immobile baseline (10–15 min); (3) mild WI (60 min).

ICP, rCBF, locomotion and video traces were processed in MATLAB. rCBF and ICP traces were resampled from 500 and 33 Hz to 1 Hz and smoothed with a median-moving window over 60 s. The rate of change was calculated as the first derivative of single ICP and rCBF traces over a 60 s timespan, smoothed with a median-moving window over 5 min. The first derivative was then average over every 10 min time blocks from mild-WI initiation.

4.5 | 2PLSM

Imaging experiments were performed in one single session per mouse 3–4 weeks after surgical recovery. Before imaging, mice were lightly sedated with isoflurane. Buprenorphine (0.1 mg/kg) was administered intraperitoneally. For vascular imaging, a heparin treated saline filled (5% heparin, LEOPharma) catheter (30G needle connected to a polyethylene PE10 tube) was inserted in the tail vein after application of local analgesia (bupivacaine, 5 mg/mL). 50 μ L of filtered (0.22 μ m pore size) 70,000 MW Texas Red-labeled dextran (0.5%, Thermo-Fisher Scientific), were injected intravenously and the mouse was head-fixed. Before imaging, mice were lightly sedated with isoflurane and buprenorphine (0.1 mg/kg).

2PLSM microscopy was performed with a Bruker/Prairie Ultima-IV, previously described in detail (Enger et al., 2017). We used a water-immersion Nikon $\times 16$ (0.8 NA) objective (CFI75 LWD 16XW). FOVs of $862 \times 862 \mu\text{m}^2$ were used for bolus tracking and Z-series, $132 \times 132 \mu\text{m}^2$ for particle velocimetry, and $246 \times 246 \mu\text{m}^2$ for Ca^{2+} imaging. We used an excitation wavelength of 900 nm (Spectra-Physics InSight DeepSee laser). Surveillance video and disc movement were recorded using a LabVIEW interface (National Instruments).

To distinguish arteries, capillaries and veins, a bolus of 50 μ L of 0.5% 70,000 MW Texas Red-labeled dextran was injected during a ~ 6.5 frame per second time-scan of pial blood vessels, followed by a 400 μ m volumetric angiogram starting from the pial surface for the reconstruction of vessel anatomy.

We used a fluorescent-bolus tracking approach for quantification of capillary flow dynamics (Gutiérrez-Jiménez et al., 2016). This method relies on the acquisition of a concentration-time curve (CTC) of an intravenously injected fluorescent tracer during its passage from arterial input to venous output. A scan path was defined passing through pial vessels, arterioles, venules and capillaries. One bolus tracking consisted of 30 μ L 70,000 MW Texas Red-labeled dextran injected intravenously during line scans acquisition (line period: 8–12 ms). Seven bolus tracking scans were performed on the same FOV over the entire protocol (3–4 h) at the following timing: two at baseline (~ 60 and ~ 30 min before WI) and four after WI every 10 min. Astrocytic Ca^{2+} signals were acquired at 30 Hz. A FOV was

imaged at baseline (100–200 μm below surface) and every 15 min after mild-WI.

4.6 | Post processing of bolus tracking data

MTT and CTH were obtained from modeling the concentration-time-curves (CTC) from the bolus tracking scans, as previously described in detail (Gutiérrez-Jiménez et al., 2016). Briefly, the signal intensity from paired artery-vein CTC curves were modeled with a vascular transport function which parametrizes the amount of fluorophore reaching the venous output as a function of time after a theoretically instantaneous arterial passage (Gutiérrez-Jiménez et al., 2016). From each vascular pair's gamma distribution, we extracted the mean plasma transit time within the capillary network ($\text{MTT} = \alpha\beta$, an inverse index of mean capillary flow) and the variance of transit times, referred in our work as blood flow heterogeneity ($\text{CTH} = \sqrt{\alpha\beta}$) (Gutiérrez-Jiménez et al., 2016; Rasmussen et al., 2015).

All image analyses were done in MATLAB (version R2017a; MathWorks, Inc.). Capillary flow parameters were defined as follows: MTT is a direct estimate of microvascular CBF, to which it is related by the central volume theorem ($\text{MTT} = V_{\text{cap}}/\text{CBF}$, V_{cap} : cerebral capillary volume) (Angleys et al., 2015). CTH is a measure of the variability of erythrocyte transit times during their passage through the same capillary network, which expresses the degree of flow heterogeneity of the microvascular bed. We estimated the coefficient of variance ($\text{RTH} = \text{CTH}/\text{MTT}$) to evaluate the active regulation of the capillary flow distribution following changes in MTT.

4.7 | Processing of microvascular line scan data

We used particle velocimetry to quantify individual capillary hemodynamics parameters (RBC flux, and velocity) and arteriolar flow (Stefanovic et al., 2008). Four FOVs with 2–6 capillaries each, randomly selected (depth: 100–200 μm) and one FOV with 1 penetrating arteriole (first branching order, depth: 80–120 μm) were scanned in each mouse. Both estimations were done on MATLAB with a sliding window approach of 500 ms time segments with an overlap of 90%. Noise artifacts were reduced using a 2-D median-filter on the raw data and outliers were removed using a moving standard deviation threshold (5 SD) on the calculated velocities and flux values. Linear density was calculated from the ratio mean RBC Flux/mean RBC velocity for every unique capillary. Linear density values above 400 cells/mm, were removed as this represents an unrealistic erythrocytes / plasma ratio (Gutiérrez-Jiménez et al., 2016). Coefficient of variance for RBC flux and velocity was calculated between vessels per time point.

4.8 | Quantification of astrocytic Ca^{2+} signaling

All astrocytic Ca^{2+} signal and behavioral analyses were performed with MATLAB (version R2017a; MathWorks). Imaging time series

were corrected for motion artifacts using the NoRMCorre movement correction algorithm (Pneumatikakis & Giovannucci, 2017). We then analyzed astrocytic Ca^{2+} transients using the event-based astrocytic Ca^{2+} signaling region-of-activity (ROA) algorithm from the Begonia toolbox (Bjørnstad et al., 2021; Bojarskaite et al., 2020). Four times the median standard deviation of the variance stabilized data plus the baseline value for a pixel was then used to calculate a threshold for signal detection for each pixel. Once the time series had been binarized into signal and non-signal, adjoining x-y-t voxels were connected to ROAs. ROAs with a spatial extent of less than three pixels per frame and duration of less than three frames in time were not included in the analyses.

We calculated the extent of Ca^{2+} activity in astrocytic subcellular compartments by measuring ROA frequency and density in manually-drawn ROIs over astroglial somata, processes, and endfeet. Only endfeet ensheathing capillary vessels, and not arterioles or venules, were selected. We only analyzed astrocytic Ca^{2+} signaling from quiet wakefulness of at least 5 s duration, defined as absence of whisking and locomotion.

4.9 | Statistical analyses

Brain water content and ICP-rCBF data were compared with a two-way ANOVA and reported as mean \pm SEM. All 2PLSM derived data were analyzed with generalized linear mixed models (GLMM) using a gamma distribution, fixed effect: time from water intoxication, random effect: mouse identity. GLMM results are reported as GLMM estimates of the central tendency \pm standard error. Significance is indexed as follow: * $p < .05$; ** $p < .01$; *** $p < .001$.

AUTHOR CONTRIBUTIONS

Conceptualization: Luca Bordonni, Sebastian Frische, Leif Østergaard, Erlend A. Nagelhus, Ole P. Ottersen, Rune Enger. Methodology: Luca Bordonni, Eugenio Gutiérrez-Jiménez, Anna E. Thoren, Daniel M. Bjørnstad, Knut S. Åbjørnsbråten, Rune Enger. Formal analysis: Luca Bordonni, Rune Enger, Daniel M. Bjørnstad, Mette Stern, Eugenio Gutiérrez-Jiménez. Investigation: Luca Bordonni. Visualization: Luca Bordonni, Rune Enger. Data curation: Luca Bordonni. Software: Luca Bordonni, Daniel M. Bjørnstad, Knut S. Åbjørnsbråten, Rune Enger. Funding acquisition: Luca Bordonni, Erlend A. Nagelhus, Sebastian Frische, Ole P. Ottersen, Rune Enger, Luca Bordonni. Project administration: Luca Bordonni, Erlend A. Nagelhus, Rune Enger. Resources: Wannan Tang, Ole Petter Ottersen, Rune Enger. Supervision: Erlend A. Nagelhus, Sebastian Frische, Rune Enger. Writing – original draft and revision: Luca Bordonni, Rune Enger. Writing – review and editing: Luca Bordonni, Anna E. Thoren, Eugenio Gutiérrez-Jiménez, Knut S. Åbjørnsbråten, Daniel M. Bjørnstad, Mette Stern, Wannan Tang, Leif Østergaard, Sebastian Frische, Ole P. Ottersen, Rune Enger.

FUNDING INFORMATION

This study was supported by the following institutions and grants: the Danish Medical Research Council (DFF grant id: 4004-00504), the



Højmossegårdlegatet (Lægeforeningen, 2017-1064/102 KBN), Aarhus University, and the European Union's Horizon 2020 Research and Innovation program under the Marie Skłodowska-Curie Actions Grant, agreement No. 80113 (Scientia Fellowship II), The Letten Foundation, The Olav Thon Foundation, Norges forskningsråd (grant numbers #249988, #302326, #262552), Helse Midt-Norge (#28293), and Felles Forskningsutvalg (FFU, grant number #34226). We acknowledge the support by UNINETT Sigma2 AS for computational science, grant NN9279K and for making data storage available through NIRD, project NS9021K.

CONFLICT OF INTEREST STATEMENT

The authors declare no conflicts of interest.

DATA AVAILABILITY STATEMENT

The raw data and derived data that support the findings of this study and the custom code used are available from the corresponding author upon reasonable request.

ORCID

Luca Bordoni <https://orcid.org/0000-0002-2428-0874>

Eugenio Gutiérrez-Jiménez <https://orcid.org/0000-0002-7509-0720>

Wannan Tang <https://orcid.org/0000-0002-2263-6435>

Leif Østergaard <https://orcid.org/0000-0003-2930-6997>

Sebastian Frische <https://orcid.org/0000-0002-0270-3602>

Ole P. Ottersen <https://orcid.org/0000-0003-1048-219X>

Rune Enger <https://orcid.org/0000-0001-9418-7117>

REFERENCES

- Adler, S., Williams, D., & Verbalis, J. G. (1993). Effect of acute and chronic hyponatremia on blood-brain barrier function in the rat. *NMR in Biomedicine*, 6, 119–124.
- Amiry-Moghaddam, M., Otsuka, T., Hurn, P. D., Traystman, R. J., Haug, F.-M., Froehner, S. C., Adams, M. E., Neely, J. D., Agre, P., Ottersen, O. P., & Bhardwaj, A. (2003). An α -syntrophin-dependent pool of AQP4 in astroglial end-feet confers bidirectional water flow between blood and brain. *Proceedings of the National Academy of Sciences*, 100, 2106–2111.
- Angleys, H., Østergaard, L., & Jespersen, S. N. (2015). The effects of capillary transit time heterogeneity (CTH) on brain oxygenation. *Journal of Cerebral Blood Flow and Metabolism*, 35, 806–817.
- Benfenati, V., Caprini, M., Dovizio, M., Mylonakou, M. N., Ferroni, S., Ottersen, O. P., & Amiry-Moghaddam, M. (2011). An aquaporin-4/transient receptor potential vanilloid 4 (AQP4/TRPV4) complex is essential for cell-volume control in astrocytes. *Proceedings of the National Academy of Sciences of the United States of America*, 108, 2563–2568.
- Bjørnstad, D. M., Åbjørnsbråten, K. S., Hennestad, E., Cunen, C., Hermansen, G. H., Bojarskaite, L., Pettersen, K. H., Vervaeke, K., & Enger, R. (2021). Begonia – a two-photon imaging analysis pipeline for astrocytic Ca^{2+} signals. *Frontiers in Cellular Neuroscience*, 15, 681066.
- Bojarskaite, L., Bjørnstad, D. M., Pettersen, K. H., Cunen, C., Hermansen, G. H., Åbjørnsbråten, K. S., Chambers, A. R., Sprengel, R., Vervaeke, K., Tang, W., Enger, R., & Nagelhus, E. A. (2020). Astrocytic Ca^{2+} signaling is reduced during sleep and is involved in the regulation of slow wave sleep. *Nature Communications*, 11, 3240.
- Bordoni, L., Jiménez, E. G., Nielsen, S., Østergaard, L., & Frische, S. (2020). A new experimental mouse model of water intoxication with sustained increased intracranial pressure and mild hyponatremia without side effects of antidiuretics. *Experimental Animals*, 69, 92–103.
- Bordoni, L., Li, B., Kura, S., Boas, D. A., Sakadžić, S., Østergaard, L., Frische, S., & Gutiérrez-Jiménez, E. (2021). Quantification of capillary perfusion in an animal model of acute intracranial hypertension. *Journal of Neurotrauma*, 38, 446–454.
- Bragin, D. E., Bush, R. C., Müller, W. S., & Nemoto, E. M. (2011). High intracranial pressure effects on cerebral cortical microvascular flow in rats. *Journal of Neurotrauma*, 28, 775–785.
- Bragin, D. E., Statom, G., & Nemoto, E. M. (2016). Dynamic cerebrovascular and intracranial pressure reactivity assessment of impaired cerebrovascular autoregulation in intracranial hypertension. *Acta Neurochirurgica Supplement*, 122, 255–260.
- Bullock, R., Maxwell, W. L., Graham, D. I., Teasdale, G. M., & Adams, J. H. (1991). Glial swelling following human cerebral contusion: An ultrastructural study. *Journal of Neurology, Neurosurgery, and Psychiatry*, 54, 427–434.
- Cai, C., Fordsmann, J. C., Jensen, S. H., Gesslein, B., Lønstrup, M., Hald, B. O., Zambach, S. A., Brodin, B., & Lauritzen, M. J. (2018). Stimulation-induced increases in cerebral blood flow and local capillary vasoconstriction depend on conducted vascular responses. *Proceedings of the National Academy of Sciences of the United States of America*, 115, E5796–E5804.
- Carney, N., Totten, A. M., O'Reilly, C., Ullman, J. S., Hawryluk, G. W. J., Bell, M. J., Bratton, S. L., Chesnut, R., Harris, O. A., Kisson, N., Rubiano, A. M., Shutter, L., Tasker, R. C., Vavilala, M. S., Wilberger, J., Wright, D. W., & Ghajar, J. (2017). Guidelines for the management of severe traumatic brain injury, Fourth Edition. *Neurosurgery*, 80, 6–15.
- Drew, P. J., Blinder, P., Cauwenberghs, G., Shih, A. Y., & Kleinfeld, D. (2010). Rapid determination of particle velocity from space-time images using the Radon transform. *Journal of Computational Neuroscience*, 29, 5–11.
- Eftekhari, S., Westgate, C. S. J., Johansen, K. P., Bruun, S. R., & Jensen, R. H. (2020). Long-term monitoring of intracranial pressure in freely-moving rats; impact of different physiological states. *Fluids Barriers CNS*, 17, 39.
- Eilert-Olsen, M., Hjukse, J. B., Thoren, A. E., Tang, W., Enger, R., Jensen, V., Pettersen, K. H., & Nagelhus, E. A. (2019). Astroglial endfeet exhibit distinct Ca^{2+} signals during hypoosmotic conditions. *Glia*, 67, 2399–2409.
- Engedal, T. S., Hjort, N., Hougaard, K. D., Simonsen, C. Z., Andersen, G., Mikkelsen, I. K., Boldsen, J. K., Eskildsen, S. F., Hansen, M. B., Angleys, H., Jespersen, S. N., Pedraza, S., Cho, T. H., Serena, J., Siemonsen, S., Thomalla, G., Nighoghossian, N., Fiehler, J., Mouridsen, K., & Østergaard, L. (2018). Transit time homogenization in ischemic stroke – A novel biomarker of penumbral microvascular failure? *Journal of Cerebral Blood Flow and Metabolism*, 38, 2006–2020.
- Enger, R., Dukefoss, D. B., Tang, W., Pettersen, K. H., Bjørnstad, D. M., Helm, P. J., Jensen, V., Sprengel, R., Vervaeke, K., Ottersen, O. P., & Nagelhus, E. A. (2017). Deletion of aquaporin-4 curtails extracellular glutamate elevation in cortical spreading depression in awake mice. *Cerebral Cortex*, 27, 24–33.
- Enger, R., Sprengel, R., Nagelhus, E. A., & Tang, W. (2019). Multiphoton Ca^{2+} imaging of astrocytes with genetically encoded indicators delivered by a viral approach. In E. Hartveit (Ed.), *Multiphoton microscopy* (pp. 251–277). Springer New York.
- Farr, G. W., Hall, C. H., Farr, S. M., Wade, R., Detzel, J. M., Adams, A. G., Buch, J. M., Beahm, D. L., Flask, C. A., Xu, K., LaManna, J. C., McGuirk, P. R., Boron, W. F., & Pelletier, M. F. (2019). Functionalized phenylbenzamides inhibit aquaporin-4 reducing cerebral edema and improving outcome in two models of CNS injury. *Neuroscience*, 404, 484–498.
- Guild, S.-J., McBryde, F. D., & Malpas, S. C. (2015). Recording of intracranial pressure in conscious rats via telemetry. *Journal of Applied Physiology*, 119, 576–581.

- Gutiérrez-Jiménez, E., Cai, C., Mikkelsen, I. K., Rasmussen, P. M., Angleys, H., Merrild, M., Mouridsen, K., Jespersen, S. N., Lee, J., Iversen, N. K., Sakadzic, S., & Østergaard, L. (2016). Effect of electrical forepaw stimulation on capillary transit-time heterogeneity (CTH). *Journal of Cerebral Blood Flow and Metabolism*, *36*, 2072–2086.
- Haft-Javaherian, M., Fang, L., Muse, V., Schaffer, C. B., Nishimura, N., & Sabuncu, M. R. (2019). Deep convolutional neural networks for segmenting 3D in vivo multiphoton images of vasculature in Alzheimer disease mouse models. *PLoS One*, *14*, e0213539.
- Haj-Yasein, N. N., Vindedal, G. F., Eilert-Olsen, M., Gundersen, G. A., Skare, Ø., Laake, P., Klungland, A., Thorén, A. E., Burkhardt, J. M., Ottersen, O. P., & Nagelhus, E. A. (2011). Glial-conditional deletion of aquaporin-4 (Aqp4) reduces blood-brain water uptake and confers barrier function on perivascular astrocyte endfeet. *Proceedings of the National Academy of Sciences of the United States of America*, *108*, 17815–17820.
- Hall, C. N., Reynell, C., Gesslein, B., Hamilton, N. B., Mishra, A., Sutherland, B. A., O'Farrell, F. M., Buchan, A. M., Lauritzen, M., & Attwell, D. (2014). Capillary pericytes regulate cerebral blood flow in health and disease. *Nature*, *508*, 55–60.
- Huber, D., Gutnisky, D. A., Peron, S., O'Connor, D. H., Wiegert, J. S., Tian, L., Oertner, T. G., Looger, L. L., & Svoboda, K. (2012). Multiple dynamic representations in the motor cortex during sensorimotor learning. *Nature*, *484*, 473–478.
- Johnston, I. H., Rowan, J. O., Harper, A. M., & Jennett, W. B. (1973). Raised intracranial pressure and cerebral blood flow. 2. Supratentorial and infratentorial mass lesions in primates. *Journal of Neurology, Neurosurgery, and Psychiatry*, *36*, 161–170.
- Kleinfeld, D., Mitra, P. P., Helmchen, F., & Denk, W. (1998). Fluctuations and stimulus-induced changes in blood flow observed in individual capillaries in layers 2 through 4 of rat neocortex. *Proceedings of the National Academy of Sciences of the United States of America*, *95*, 15741–15746.
- Krogsgaard, A., Sperling, L., Dahlqvist, M., Thomsen, K., Vydmantaitė, G., Lauritzen, M., & Lind, B. L. (2022). Astrocytic Ca²⁺ signals partake in inhibitory neurovascular coupling in a brain state-dependent manner. *bioRxiv* [Internet]: 2022.02.23.478942 Available from: <https://www.biorxiv.org/content/biorxiv/early/2022/02/25/2022.02.23.478942>
- Leinonen, V., Vanninen, R., & Rauramaa, T. (2017). Raised intracranial pressure and brain edema. *Handbook of Clinical Neurology*, *145*, 25–37.
- Li, X., Gao, J., Ding, J., Hu, G., & Xiao, M. (2013). Aquaporin-4 expression contributes to decreases in brain water content during mouse postnatal development. *Brain Research Bulletin*, *94*, 49–55.
- Longden, T. A., Dabertrand, F., Koide, M., Gonzales, A. L., Tykocki, N. R., Brayden, J. E., Hill-Eubanks, D., & Nelson, M. T. (2017). Capillary K⁺-sensing initiates retrograde hyperpolarization to increase local cerebral blood flow. *Nature Neuroscience* [Internet], *20*, 717–726 Available from: <https://doi.org/10.1038/nn.4533>
- Madhok, D. Y., Vitt, J. R., & Nguyen, A. T. (2018). Overview of neurovascular physiology. *Current Neurology and Neuroscience Reports*, *18*, 99.
- Manley, G. T., Fujimura, M., Ma, T., Noshita, N., Filiz, F., Bollen, A. W., Chan, P., & Verkman, A. S. (2000). Aquaporin-4 deletion in mice reduces brain edema after acute water intoxication and ischemic stroke. *Nature Medicine*, *6*, 159–163.
- Mathiisen, T. M., Lehre, K. P., Danbolt, N. C., & Ottersen, O. P. (2010). The perivascular astroglial sheath provides a complete covering of the brain microvessels: An electron microscopic 3D reconstruction. *Glia*, *58*, 1094–1103.
- Melton, J. E., Patlak, C. S., Pettigrew, K. D., & Cserr, H. F. (1987). Volume regulatory loss of Na, Cl, and K from rat brain during acute hyponatremia. *The American Journal of Physiology*, *252*, F661–F669.
- Mishra, A., Reynolds, J. P., Chen, Y., Gourine, A. V., Rusakov, D. A., & Attwell, D. (2016). Astrocytes mediate neurovascular signaling to capillary pericytes but not to arterioles. *Nature Neuroscience*, *19*, 1619–1627.
- Mouridsen, K., Hansen, M. B., Østergaard, L., & Jespersen, S. N. (2014). Reliable estimation of capillary transit time distributions using DSC-MRI. *Journal of Cerebral Blood Flow and Metabolism*, *34*, 1511–1521.
- Nakayama, S., Migliati, E., Amiry-Moghaddam, M., Ottersen, O. P., & Bhardwaj, A. (2016). Osmotherapy with hypertonic saline attenuates global cerebral edema following experimental cardiac arrest via perivascular pool of aquaporin-4. *Critical Care Medicine*, *44*, e702–e710.
- Nehring, S. M., Tadi, P., & Tenny, S. (2022). *Cerebral Edema*. StatPearls Publishing.
- Nielsen, S., Nagelhus, E. A., Amiry-Moghaddam, M., Bourque, C., Agre, P., & Ottersen, O. P. (1997). Specialized membrane domains for water transport in glial cells: High-resolution immunogold cytochemistry of aquaporin-4 in rat brain. *The Journal of Neuroscience*, *17*, 171–180.
- Østergaard, L., Engedal, T. S., Aamand, R., Mikkelsen, R., Iversen, N. K., Anzabi, M., Næss-Schmidt, E. T., Drasbek, K. R., Bay, V., Blicher, J. U., Tietze, A., Mikkelsen, I. K., Hansen, B., Jespersen, S. N., Juul, N., Sørensen, J. C. H., & Rasmussen, M. (2014). Capillary transit time heterogeneity and flow-metabolism coupling after traumatic brain injury. *Journal of Cerebral Blood Flow and Metabolism*, *34*, 1585–1598.
- Østergaard, L., Jespersen, S. N., Engedahl, T., Gutiérrez Jiménez, E., Ashkanian, M., Hansen, M. B., Eskildsen, S., & Mouridsen, K. (2015). Capillary dysfunction: Its detection and causative role in dementias and stroke. *Current Neurology and Neuroscience Reports*, *15*, 37.
- Pnevmatikakis, E. A., & Giovannucci, A. (2017). NoRMCorre: An online algorithm for piecewise rigid motion correction of calcium imaging data. *Journal of Neuroscience Methods*, *291*, 83–94.
- Rasmussen, P. M., Jespersen, S. N., & Østergaard, L. (2015). The effects of transit time heterogeneity on brain oxygenation during rest and functional activation. *Journal of Cerebral Blood Flow and Metabolism*, *35*, 432–442.
- Slupe, A. M., & Kirsch, J. R. (2018). Effects of anesthesia on cerebral blood flow, metabolism, and neuroprotection. *Journal of Cerebral Blood Flow and Metabolism*, *38*, 2192–2208.
- Stefanovic, B., Hutchinson, E., Yakovleva, V., Schram, V., Russell, J. T., Belluscio, L., Koretsky, A. P., & Silva, A. C. (2008). Functional reactivity of cerebral capillaries. *Journal of Cerebral Blood Flow and Metabolism*, *28*, 961–972.
- Stokum, J. A., Gerzanich, V., & Simard, J. M. (2016). Molecular pathophysiology of cerebral edema. *Journal of Cerebral Blood Flow and Metabolism*, *36*, 513–538.
- Tang, W., Szokol, K., Jensen, V., Enger, R., Trivedi, C. A., Hvalby, Ø., Helm, P. J., Looger, L. L., Sprengel, R., & Nagelhus, E. A. (2015). Stimulation-evoked Ca²⁺ signals in astrocytic processes at hippocampal CA3-CA1 synapses of adult mice are modulated by glutamate and ATP. *The Journal of Neuroscience*, *35*, 3016–3021.
- Thrane, A. S., Rangroo Thrane, V., Zeppenfeld, D., Lou, N., Xu, Q., Nagelhus, E. A., & Nedergaard, M. (2012). General anesthesia selectively disrupts astrocyte calcium signaling in the awake mouse cortex. *Proceedings of the National Academy of Sciences of the United States of America*, *109*, 18974–18979.
- Thrane, A. S., Rappold, P. M., Fujita, T., Torres, A., Bekar, L. K., Takano, T., Peng, W., Wang, F., Thrane, V. R., Enger, R., & Haj-Yasein, N. N. (2011). Critical role of aquaporin-4 (AQP4) in astrocytic Ca²⁺ signaling events elicited by cerebral edema. *Proceedings of the National Academy of Sciences*, *108*, 846–851.
- Toft-Bertelsen, T. L., Larsen, B. R., Christensen, S. K., Khandelia, H., Waagepetersen, H. S., & MacAulay, N. (2021). Clearance of activity-evoked K⁺ transients and associated glia cell swelling occur independently of AQP4: A study with an isoform-selective AQP4 inhibitor. *Glia*, *69*, 28–41.
- Uhlirva, H., Kılıç, K., Tian, P., Thunemann, M., Desjardins, M., Saisan, P. A., Sakadžić, S., Ness, T. V., Mateo, C., Cheng, Q., Weldy, K. L., Razoux, F.,

- Vandenberghe, M., Cremonesi, J. A., Ferri, C. G., Nizar, K., Sridhar, V. B., Steed, T. C., Abashin, M., ... Devor, A. (2016). Cell type specificity of neurovascular coupling in cerebral cortex. *Elife*, 5, e14315. Available from: <https://doi.org/10.7554/eLife.14315>
- Vajda, Z., Pedersen, M., Doczi, T., Sulyok, E., & Nielsen, S. (2004). Studies of mdx mice. *Neuroscience*, 129, 993–998.
- Vajda, Z., Pedersen, M., Füchtbauer, E.-M., Wertz, K., Stødkilde-Jørgensen, H., Sulyok, E., Dóczi, T., Neely, J. D., Agre, P., Frøkiær, J., & Nielsen, S. (2002). Delayed onset of brain edema and mislocalization of aquaporin-4 in dystrophin-null transgenic mice. *Proceedings of the National Academy of Sciences of the United States of America*, 99, 13131–13136.
- Yang, B., Zador, Z., & Verkman, A. S. (2008). Glial cell aquaporin-4 overexpression in transgenic mice accelerates cytotoxic brain swelling. *The Journal of Biological Chemistry*, 283, 15280–15286.

SUPPORTING INFORMATION

Additional supporting information can be found online in the Supporting Information section at the end of this article.

How to cite this article: Bordoni, L., Thoren, A. E., Gutiérrez-Jiménez, E., Åbjørsbråten, K. S., Bjørnstad, D. M., Tang, W., Stern, M., Østergaard, L., Nagelhus, E. A., Frische, S., Ottersen, O. P., & Enger, R. (2023). Deletion of aquaporin-4 improves capillary blood flow distribution in brain edema. *Glia*, 71(11), 2559–2572. <https://doi.org/10.1002/glia.24439>